

van der Waals Epitaxy of Earth-Abundant Zn_3P_2 on Graphene for Photovoltaics

Rajrupa Paul, Nicolas Humblot, Simon Escobar Steinvall, Elias Zsolt Stutz, Shreyas Sanjay Joglekar, Jean-Baptiste Leran, Mahdi Zamani, Cyril Cayron, Roland Logé, Andres Granados del Aguila, Qihua Xiong, and Anna Fontcuberta i Morral*



Cite This: <https://dx.doi.org/10.1021/acs.cgd.0c00125>



Read Online

ACCESS |



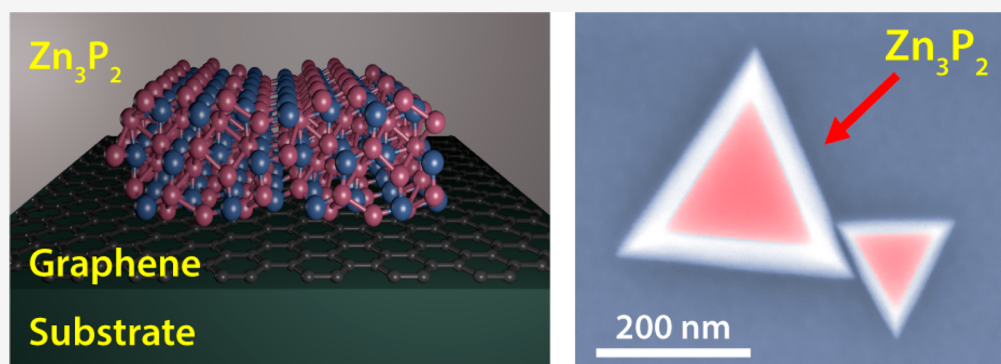
Metrics & More



Article Recommendations



Supporting Information



ABSTRACT: Earth-abundant semiconducting materials are a potential solution for large-scale deployment of solar cells at a lower cost. Zinc phosphide (Zn_3P_2) is one such Earth-abundant material with optoelectronic properties suitable for photovoltaics. Herein, we report the van der Waals epitaxy of tetragonal Zn_3P_2 ($\alpha\text{-Zn}_3\text{P}_2$) on graphene using molecular beam epitaxy. The growth on graphene progresses by the formation of Zn_3P_2 triangular flakes, which merge to form a thin film with a strong (101) crystallographic texture. Photoluminescence from the Zn_3P_2 thin films is consistent with previously reported Zn_3P_2 . This work demonstrates that the need for a lattice-matched substrate can be circumvented by the use of graphene as a substrate. Moreover, the synthesis of high-quality Zn_3P_2 flakes and films on graphene brings new material choices for low-cost photovoltaic applications.

INTRODUCTION

The global energy consumption continues to severely impact the world's climatic conditions, and this necessitates a firm shift toward clean and sustainable sources of energy. Earth-abundant semiconducting materials could be beneficial for the purpose of low-cost, large-scale deployment of photovoltaics.^{1,2} Zn_3P_2 is an Earth-abundant semiconductor with promising optoelectronic properties.^{3–5} Zn_3P_2 has a high absorption coefficient ($>10^4 \text{ cm}^{-1}$)⁶ in the visible part of the electromagnetic spectrum and long minority-carrier diffusion length ($>5 \mu\text{m}$).⁷ The reported band gap of Zn_3P_2 lies close to the theoretical maxima of the Shockley–Queisser limit,⁸ making it a suitable candidate for photovoltaics.^{9,10} The highest solar energy conversion efficiency ($\sim 6\%$) was reported by Bhushan et al. for Mg- Zn_3P_2 based solar cells.¹¹

Since 1981, there has been no report on the improvement of efficiency for Zn_3P_2 -based solar cells. One of the major issues associated with Zn_3P_2 is its large lattice parameter ($a = 8.089 \text{ \AA}$, $c = 11.45 \text{ \AA}$),¹² which makes high-quality epitaxial growth suitable for solar cell application challenging.¹³ Furthermore, the choice of substrate is limited due to the large linear thermal

expansion coefficient ($1.4 \times 10^{-5} \text{ K}^{-1}$)¹⁴ of Zn_3P_2 .¹⁵ Cracks were observed on Zn_3P_2 thin films grown at high temperatures ($\geq 600 \text{ }^\circ\text{C}$) on a large number of commercially available substrates.¹⁵ Additionally, the formation energies of zinc vacancies and phosphorus interstitials are very low in Zn_3P_2 , which makes the material intrinsically p-type.^{16,17} The intrinsic p-type nature of Zn_3P_2 in principle rules out the formation of low-resistive homojunction solar cells. And most of the Zn_3P_2 solar cells are based on heterojunction or Schottky junction.^{11,18}

In 1984, Atsushi Koma introduced the concept of van der Waals epitaxy (vdWE). He demonstrated the growth of an epitaxial thin film on a substrate with over 20% lattice mismatch by avoiding the formation of covalent bonds at the

Received: January 29, 2020

Revised: April 9, 2020

Published: April 9, 2020

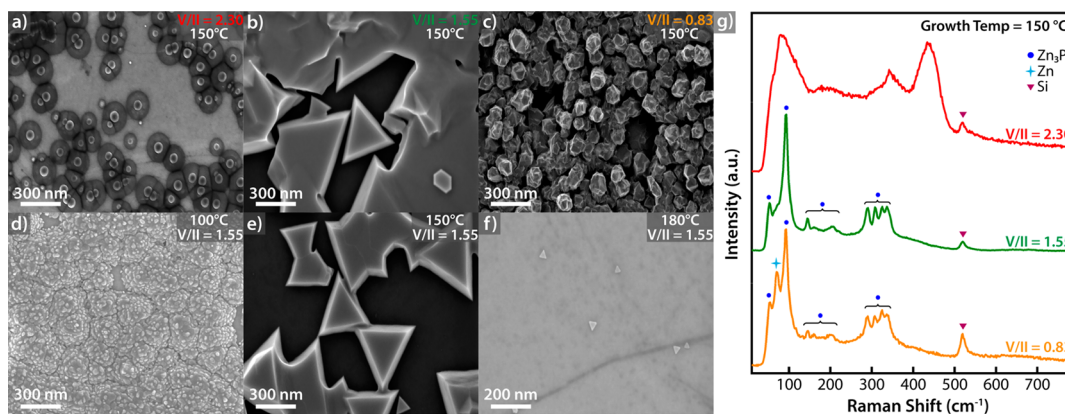


Figure 1. (a–f) Representative scanning electron micrographs of growths of Zn₃P₂ on graphene as a function of temperature and V/II ratio; (g) room temperature Raman spectra of samples shown in a–c, indicating that for V/II = 1.55 crystalline Zn₃P₂ is formed, while for lower V/II ratios crystalline zinc is found in addition, and for higher V/II ratios the material is amorphous.

interface.¹⁹ The advantage of vdWE is the use of substrates with no dangling bonds, such as two-dimensional materials (e.g., graphene) or bulk layered materials (e.g., mica).^{20,21} Because of the absence of dangling bonds at the surface of a van der Waals substrate, the growth of the overlayer proceeds without the formation of covalent bonds at the interface. van der Waals bonds originate from the dipolar interactions between atoms. Compared to covalent bonds, the van der Waals bonds are much weaker, and this gives an unstrained epitaxial overlayer growth with a defect-free interface on a highly lattice-mismatched substrate. Hence, vdWE could be a suitable method to overcome the limitation of lattice-matched substrates for the growth of high-quality epitaxial material. Graphene is widely used for vdWE due to its two-dimensional nature as well as its high electrical and thermal conductivities,^{22,23} optical transparency,²⁴ and high mechanical strength and flexibility.^{25–27} The recent advances in the synthesis technique of high-quality graphene have made it possible to fabricate large-area polycrystalline graphene substrates at a lower cost.^{28,29} Graphene can function as a low-cost, transparent, and flexible electrode, which can be exploited for the fabrication of Zn₃P₂-graphene junction-based solar cells. Vazquez-Mena et al. demonstrated a field-effect solar cell using graphene that formed a tunable junction barrier with Zn₃P₂.³⁰ This opens an avenue for the integration of functional material on graphene to create a new hybrid material system.

Bosco et al.¹³ demonstrated the growth of Zn₃P₂ on GaAs substrates by congruently sublimating Zn₃P₂. We believe that the use of congruent sublimation can come at the expense of controlling the stoichiometry of the material in a precise manner. As an example, Suda et al. reported the growth of n-type Zn₃P₂ by using elemental source MBE.³¹ They attributed the n-type behavior of Zn₃P₂ on the zinc-rich growth conditions. Additionally, the use of MBE has some advantages over other growth techniques commonly used for Zn₃P₂ growth.^{32,33} MBE uses high purity source materials and an ultrahigh vacuum growth environment, which ensures low impurity incorporation.

In this work, we demonstrate the growth of high-quality Zn₃P₂ on graphene with vdWE using MBE, as demonstrated by the structural and optical properties. The optimum growth parameters were established by varying the temperature, pressure, and flux ratio in our system. We present the growth

mechanism, based on the observation of how the film evolves with growth time. This work shows a direct and efficient way to integrate Zn₃P₂ on graphene.

RESULTS AND DISCUSSION

We start by reporting the influence of growth parameters on the morphology and the composition of Zn₃P₂ grown on graphene. The variation of the V/II ratio could potentially lead to the formation of different compounds, such as ZnP₂, Zn₃P₂, and even intermediate amorphous compounds (a-Zn_xP_y).^{34,13} The reported V/II ratio in this work corresponds to the ratio between the values of Zn and P₂ beam equivalent pressure (BEP), and the temperatures correspond to the manipulator temperature. Electron microscopy characterization of the initial stages of growth provides information on the morphology of the grown material. Figure 1a–f displays the scanning electron microscopy (SEM) images of Zn₃P₂ samples obtained at different temperatures and V/II ratios. The effect of the V/II ratio at 150 °C is shown in the SEM micrographs of Figure 1a–c. For V/II ≥ 2.30, the morphology of the grown material is spherical with no distinct crystal facets. When the V/II ratio is maintained between 1.30 and 1.70, we observe a change in morphology. Crystalline triangular flakes are formed on graphene. These triangular flakes are not all randomly oriented as can be observed from the SEM images. When the V/II ratio is decreased to a value below 0.83, the triangular flakes change to a dense columnar-like growth. The influence of temperature on morphology at a given V/II ratio is shown in the SEM images of Figure 1d–f. At temperatures ≤ 100 °C, we observe irregularly shaped clusters with metal-like aggregates on top, as shown in Figure 1d. As the temperature is increased to 150 °C, crystalline triangular flakes start to appear. By further increasing the temperature to 180 °C, there is a substantial decrease in the growth rate, and the deposition is sparse. However, the triangular morphology is preserved at 180 °C. We attribute the drastic reduction in the growth rate at higher temperatures to the increased adatom desorption.

Figure 1g presents the room temperature Raman spectra of the samples grown at 150 °C at three different V/II ratios. At a V/II ratio of 2.30, the Raman spectrum is composed of broad peaks. This is consistent with the amorphous nature of the material, which is evident from its morphology (Figure 1a). The Raman peaks become sharper for lower V/II ratios. The

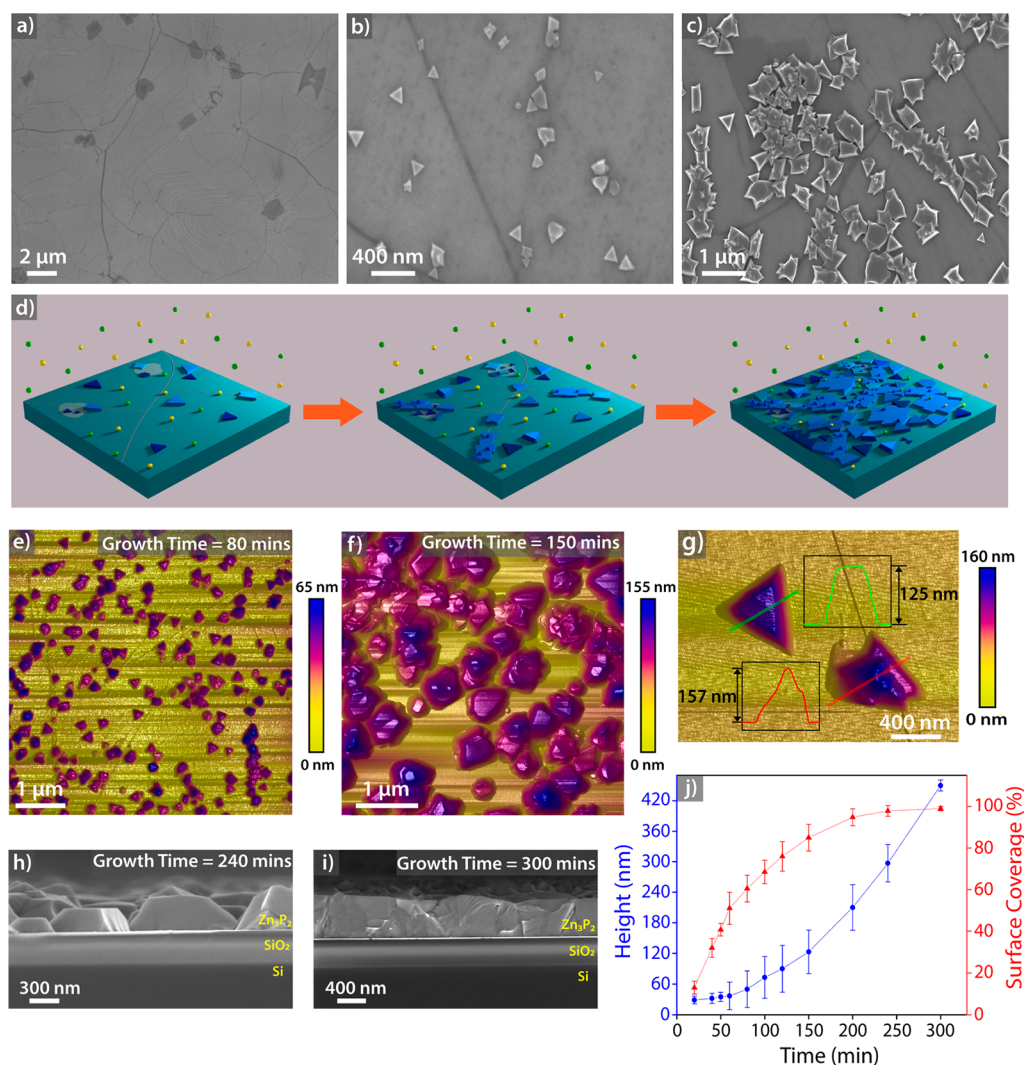


Figure 2. (a–c) SEM images of (a) commercial graphene, (b) Zn_3P_2 triangular flakes grown on graphene after growing for 20 min, and (c) Zn_3P_2 triangular flakes grown on graphene after growing for 90 min; (d) schematic representation of the growth evolution of Zn_3P_2 on graphene; (e–f) AFM images of Zn_3P_2 grown on graphene for (e) 80 min and (f) 150 min; (g) highlights two different morphologies of Zn_3P_2 grown on graphene; (h–i) cross-sectional SEM images of Zn_3P_2 grown on graphene for (h) 240 min and (i) 300 min; (j) plot showing the time evolution of the surface coverage (red triangular symbol) and vertical dimensions (blue circular symbol) of Zn_3P_2 flakes on graphene; the solid lines in the graph is a guide to the eye.

bands are located around the spectral zone where one would expect for $\alpha\text{-Zn}_3\text{P}_2$.^{35,36} Both for $V/II = 1.55$ and 0.83 , we observe a group of peaks in the range between 50 cm^{-1} and 380 cm^{-1} , with no first-order Raman active phonons present at wavenumbers higher than 380 cm^{-1} , similar to the reports from Pangilinan et al. for $\alpha\text{-Zn}_3\text{P}_2$.³⁵ This demonstrates the formation of crystalline $\alpha\text{-Zn}_3\text{P}_2$ on graphene. For $V/II = 0.83$, we detect an additional peak at 71 cm^{-1} , which is related to the presence of crystalline Zn. The presence of Zn could explain the modification in the morphology of the sample, which could be due to the formation of Zn aggregates³⁷ (Figure 1c). The intensity of the Raman peak at 71 cm^{-1} increases when the V/II ratio is further lowered (see Supporting Information (SI) Figure S1). The presence of Zn has been further confirmed by X-ray diffraction (XRD) measurements, as shown in Figure S2. We find peaks corresponding to the (002) and (101) planes of Zn, along with the XRD peaks from crystalline $\alpha\text{-Zn}_3\text{P}_2$. At the given growth temperature, Zn has a low sticking coefficient on graphene.^{38,39,13} However, the formation of Zn aggregates could imply that first a Zn_3P_2 layer is formed on graphene,

which subsequently leads to the change in adsorption behavior of Zn. This explains the presence of both Zn and $\alpha\text{-Zn}_3\text{P}_2$ peaks in the Raman spectra and the XRD measurement. It is further corroborated by the SEM image shown in the inset of Figure S2, and a clear Zn_3P_2 layer is present on top of which Zn aggregates are formed.

The growth window for crystalline $\alpha\text{-Zn}_3\text{P}_2$ on graphene is relatively narrow, unlike other semiconducting materials grown on graphene, which have robust growth conditions.^{40,41} The optimum temperature range is between 150 and $170\text{ }^\circ\text{C}$, with an optimum V/II ratio between 1.3 and 1.7 . An additional dependence on the total flux was also observed (see SI, Figure S3a–c). At the optimal temperature and V/II ratio, an increase in total flux leads to an expected increase in the overall growth rate; this is due to a higher surface adatom density, which causes an increase in nucleation density. Thus, the growth of Zn_3P_2 on graphene is susceptible to temperature, V/II , and total flux. All the studies reported hereafter are done on the samples grown at $150\text{ }^\circ\text{C}$ with a V/II ratio of 1.55 . The P_2 BEP was maintained at 7.50×10^{-7} Torr unless specified otherwise.

Figure 2a shows a representative top-view SEM image of the commercial monolayer graphene on SiO₂/Si wafer used in this work. The contrast in the image is related to the presence of grain boundaries, multilayers, wrinkles, and folds on graphene.^{42–45} Such features are common for graphene grown by CVD on a polycrystalline copper substrate.^{44,46} The defects on graphene play a critical role in adsorption, and nucleation of adatoms as the sticking coefficient of adatoms is significantly different at these sites.^{43,47} The nucleation probability of a new layer is higher at the defect sites than on pristine graphene due to their higher chemical reactivity.^{43,48} The growth on pristine graphene is highly suppressed due to the lack of dangling bonds.³⁸ Figure 2b–c elucidates the growth evolution of Zn₃P₂ on graphene substrate with time. As the growth progresses, the Zn₃P₂ flakes accumulate at the grain boundaries and other defect sites, which leads to the formation of compact islands with an irregular shape at these sites. At this stage of growth, the island formation tends to be sparse away from these defect sites, preserving the triangular shape of the flakes. The growth at the folds and grain boundaries on graphene traces their linear morphology.⁴⁵ In the case of multilayer graphene, the growth traces their patch-like morphology.^{49–51} The defect sites have strikingly different growth behavior, as precursors exhibit a higher sticking coefficient at these sites.^{45,52} Overall, we find that the growth of Zn₃P₂ on commercial graphene is highly impacted by the defects, creating distinct growth regimes simultaneously on the same substrate. Figure 2d depicts our understanding of the growth mechanism of Zn₃P₂ on commercial graphene. The growth starts with the formation of small triangular flakes of Zn₃P₂ all over the substrate. With time, the nucleation density along the grain boundaries and other defect sites increases, which causes a preferential deposition of Zn₃P₂. Eventually, the triangular flakes grow in dimension to form several micron large Zn₃P₂ islands. Finally, all Zn₃P₂ islands merge with one another, forming a compact continuous film with a coarse surface.

In order to determine the growth rate of Zn₃P₂ film, we performed a growth time series. SEM and atomic force microscopy (AFM) were used to study the vertical and lateral dimensions of the Zn₃P₂ triangular flakes as a function of time. Figure 2e–g corresponds to representative AFM images as a function of the growth time. In the early stages of growth, when the surface coverage is relatively low, the triangular flakes are well dispersed on the substrate, as illustrated in Figure 2e. Some of the flakes are seen to merge mostly along the grain boundaries of graphene. The average height of these flakes after 80 min of growth is 60 nm. The lateral dimension has a significant size distribution. For a longer duration of growth, the flakes start to lose its distinct triangular shape as they merge with the other neighboring flakes. The average height of the Zn₃P₂ flakes after 150 min growth is 130 nm. Figure 2g illustrates the morphology of the top facet of the flake at two different growth sites. The Zn₃P₂ island deposited along the fold in graphene has an irregular base with a pyramid-like top facet (highlighted with a red line). The irregular base of the growing island is due to the merging of two or more triangular flakes in the initial phase of the growth. The pyramid-like facets are mainly observed on top of Zn₃P₂ islands and are denser at the folds, wrinkles, and defect sites. This type of growth behavior could be due to localized growth front pinning, which occurs at the contact point between two or more growing islands^{53,54} or could be attributed to interfacial disloca-

tions.^{54–56} In contrast, Zn₃P₂ growth away from the fold exhibits a triangular shape with a smooth top surface (highlighted with a green line). This illustrates the difference in the morphology of Zn₃P₂ islands based on their nucleation site.

For longer growth times, the height of the layers was determined by cross-section SEM, as shown in Figure 2h–i. For a growth duration of 240 min, Zn₃P₂ islands were obtained with an average thickness of 300 nm (see Figure 2h). Finally, for a growth duration of 300 min and longer, the adjoining Zn₃P₂ islands merge to form a continuous film. The thickness of the film obtained for 300 min of growth time is 450 nm. The film surface is highly faceted, as seen in Figure 2i.

The time evolution of surface coverage and vertical dimensions of the Zn₃P₂ flakes and islands is plotted in Figure 2j. The error bars in the graph represent the broad size distribution of Zn₃P₂ flakes on graphene. We observe a dominant lateral growth at the initial stages of growth, which slows down over time, whereas the vertical growth rate increases significantly with time. For the first 20 min of growth, small triangular Zn₃P₂ flakes were observed with an average lateral dimension of 95 nm and an average height of 35 nm. After further 60 min of growth, the average lateral dimension changes to 200 nm, and the average vertical dimension changes to 60 nm. This indicates that, in the initial stages of growth when the surface coverage is low, the Zn₃P₂ flakes grow primarily laterally. This is due to the adatom kinetics: the adatom supply to the growing flakes is mainly by adsorption onto the graphene substrate followed by surface diffusion. As the migration energy barrier is low on graphene, the adatom can diffuse over a longer distance before being incorporated into an energetically favorable growing site.^{38,39} After 150 min of total growth time, the average lateral dimension is 530 nm, and the average vertical dimension is 130 nm. After an additional 60 min of growth, the average lateral dimension changes to 570 nm, and the vertical dimension changes to 235 nm. It is clear that at this stage of growth, the vertical growth rate is much higher in comparison to the lateral growth rate. Indeed, at a surface coverage of approximately 80%, a significant number of Zn₃P₂ islands merge or are closely spaced. Hence, for growth durations longer than 150 min, it is difficult to measure the lateral dimensions of individual Zn₃P₂ flakes. For longer growth durations, we compare the surface coverage with the vertical dimension of the islands. An 80% surface coverage is achieved in first 150 min; however, a further 150 min of growth is required to achieve 100% surface coverage. The significant slowdown of the lateral growth rate and the increase in vertical growth rate are primarily due to two reasons. First, at a growth stage with high surface coverage, most of the adatoms are incorporated directly onto the Zn₃P₂ islands, which have a higher absorption coefficient than graphene. And only a small fraction of material is deposited into the trenches between these growing islands, thus increasing the vertical growth rate and slowing down the surface coverage. Second, an important factor that aids the vertical growth rate during the epitaxial growth of three-dimensional materials is the so-called Ehrlich–Schwoebel (ES) barrier.^{57,58} The ES barrier hinders the step-down diffusion of adatoms landing on a terrace.⁵⁸ The presence of ES barrier causes an accumulation of atoms on the top-facet of an island, which favors the vertical growth. One should note that there is a significant deviation in the growth rate at the grain boundaries, multilayer graphene, and other defect sites.

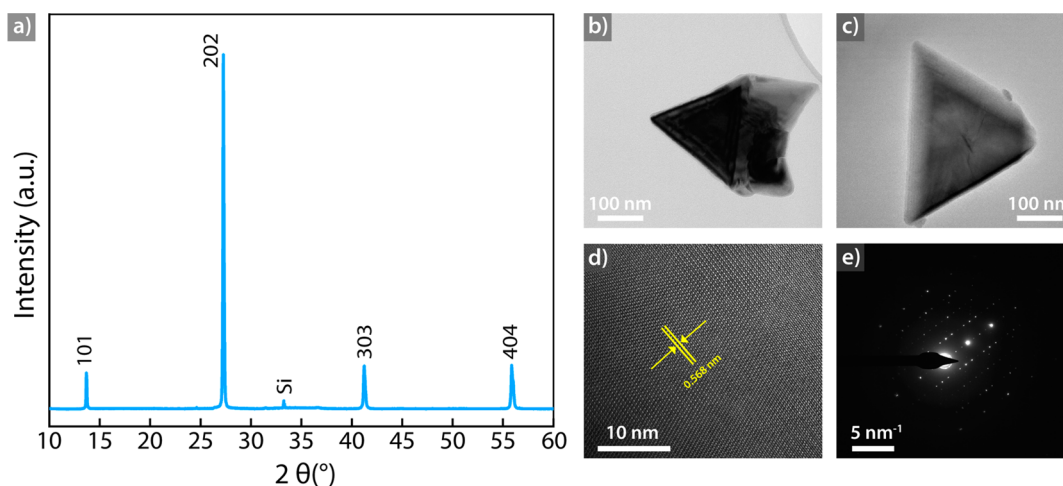


Figure 3. (a) XRD pattern of a Zn_3P_2 film showing the tetragonal structure and a preferential orientation. Only $\{101\}$ family of planes are observed in the pattern; (b–c) Bright-field TEM images of the triangular Zn_3P_2 flake grown on graphene; (d) HRTEM image of the triangular Zn_3P_2 flake, showing a d -spacing of 0.568 nm; (e) electron diffraction pattern obtained from the Zn_3P_2 flake along the $[210]$ zone axis.

We believe the growth on graphene could be improved by suppressing nucleation density at the defect sites. This could be achieved by increasing the growth temperature or by decreasing the growth pressure. However, as mentioned before, the growth rate drops significantly by increasing the temperature from 150 to 180 °C. A similar effect is observed when the pressure is decreased. It is mainly because Zn and P have a very low sticking coefficient on graphene at elevated temperatures.³⁸ Alternatively, postgrowth annealing could be used to improve the grown film.^{59,60} However, it was reported by Bosco et al. that the desorption of Zn occurs at a temperature above 250 °C.¹³ This limits the temperature range for annealing and hence compromises the quality of the film. In this work, we mainly focus on a one-step growth method, where a fixed temperature, V/II value, and total flux were used throughout the growth. We also attempted a two-step growth method.⁴⁰ Here, we induced first the nucleation at 150 °C and followed by a high-temperature growth step (190 °C). One should note, for the two-step growth, a negligible change in the Zn_3P_2 thin film was observed. And even after 300 min of growth, we did not obtain full coverage. Pyramidal top facets were observed for both one-step growth and two-step growth methods.

The X-ray diffraction (XRD) measurement done on the grown Zn_3P_2 film is shown in Figure 3a. Four main peaks resolved at 13.54°, 27.10°, 41.09°, and 55.80° correspond to the reflections 101, 202, 303, and 404, respectively in the tetragonal phase of Zn_3P_2 . The indexing was done using the reference ICDD file no. 01-073-4212.⁶¹ Additionally, a low-intensity peak at 33.11° was observed, which is attributed to the substrate. The lattice parameters were calculated from profile fitting of the XRD peaks, and $a = 8.087$ Å and $c = 11.43$ Å were obtained, which gives a $c/a = 1.41$. This is very close to the reported bulk lattice parameter of Zn_3P_2 .^{61,62} The symmetrical θ - 2θ scan gives information on the planes that are parallel to the substrate surface. Only the peaks associated with the $\{101\}$ family of planes are detected. This indicates that the Zn_3P_2 film has a preferential orientation parallel to the graphene surface. The film is thus highly textured and composed solely of the tetragonal Zn_3P_2 phase. These results were also confirmed by electron backscattered diffraction (EBSD) measurements, which showed the same preferentially

orientation with respect to the graphene substrate (see SI, Figure S4). EBSD measurements were performed on samples that were grown for a shorter period, with less than 60% surface coverage, whereas the XRD measurements were done on samples grown for a long period, with full surface coverage. Both samples gave the same directional dependence, indicating that the Zn_3P_2 islands maintain the same growth direction over time. Given the tetragonal crystal structure of Zn_3P_2 , the 3-fold symmetry of the triangular flake can only be the result of a pseudosymmetry. Indeed, the Zn_3P_2 crystal structure is often defined as a pseudocubic crystal system,⁶² with c/a exactly equal to $\sqrt{2}$. When the tetragonal crystal system is transformed into the pseudocubic crystal system, the (101) plane is transformed to the (111) plane, which explains the morphology of the flakes. For a cubic system, the $[111]$ 3-fold growth direction is the most common on a hexagonal (0001) substrate.^{63–65} The van der Waals interaction between the grown Zn_3P_2 and graphene is confirmed by its crystallographic texture; as a (101) fiber texture is present, it indicates there is a complete degree of freedom on the rotation angle around the normal of the (101) plane of Zn_3P_2 , whereas a classical epitaxial relation would have resulted in a strict coherent orientation relationship of the grown material with the substrate. The Zn_3P_2 structure was further investigated using transmission electron microscopy (TEM), shown in Figure 3b–c. For this, Zn_3P_2 flakes were transferred to a TEM grid by pressing the grid on the sample. A small force is required to remove them, due to the weak van der Waals forces attaching the flakes on the graphene. The flake exhibits a 3 nm thick native amorphous oxide at the surface. This native oxide is formed upon exposure to atmospheric conditions. Figure 3d shows a representative HRTEM micrograph. It reveals a defect-free single crystalline Zn_3P_2 triangular flake. From these measurements, we deduced the spacing between the (002) planes. We obtain 5.68 Å, which corresponds to $c = 11.36$ Å, which is in close agreement with the XRD results. The electron diffraction (Figure 3e) further confirms the single-crystalline nature of the Zn_3P_2 triangular flake. The diffraction pattern is in good agreement with the $[210]$ zone axis of α - Zn_3P_2 .

Katsube et al. had previously demonstrated the fabrication of (101) oriented Zn_3P_2 film by phosphidation of Zn film.⁶⁶ They compared the electrical resistivity of the (101) oriented Zn_3P_2

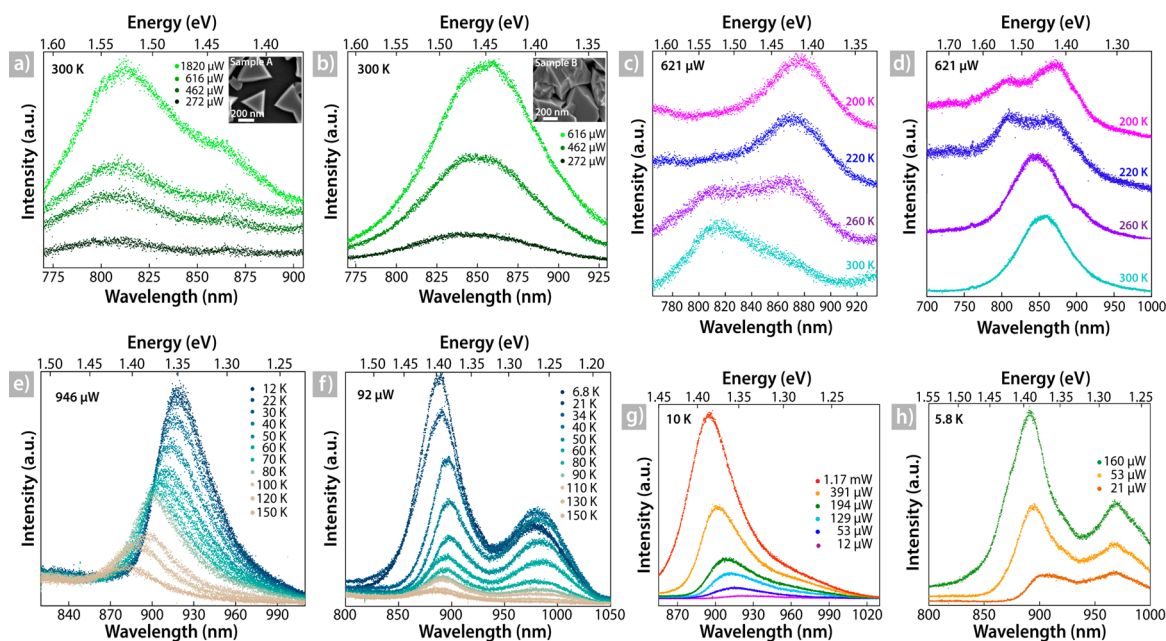


Figure 4. (a–b) PL spectra at room temperature excited with 633 nm illumination with different powers (a) of sample A, which is Zn_3P_2 grown on graphene for 100 min; inset shows the SEM image of sample A, (b) of sample B, which is Zn_3P_2 grown on graphene for 250 min; inset shows the SEM image of sample B; (c–d) PL spectra at temperatures from 300 to 200 K excited with 633 nm illumination at 621 μW of (c) sample A, and (d) sample B; (e–f) PL spectra done by decreasing the temperature below 200 K excited with 532 nm illumination (e) at 946 μW on sample A, and (f) at 92 μW on sample B; (g–h) PL spectra at cryogenic temperature using different powers (g) on sample A at 10 K excited with 633 nm illumination, and (h) on sample B at 5.8 K excited with 532 nm illumination.

film with a differently oriented Zn_3P_2 film, and they observed the lowest resistivity for the (101) orientation. The vdWE of Zn_3P_2 on graphene is a phosphidation-free method to obtain the low resistive (101) orientated Zn_3P_2 film, which is beneficial for solar cell device fabrication.

The optical properties of Zn_3P_2 are of great interest, given the potential application in photovoltaics.¹¹ There has been a long-standing controversy regarding the fundamental gap of the material.^{9,67,68} Recently, a study done by Kimball et al. showed that there is a fundamental indirect bandgap at 1.38 eV and a direct bandgap at 1.50 eV.¹⁰ The presence of both indirect and direct bandgap in close proximity is deemed beneficial in solar cell material, as the indirect bandgap could result in longer carrier lifetimes and diffusion lengths, whereas the close-lying direct bandgap could provide high photo-generation efficiencies. In order to understand the optical properties of Zn_3P_2 grown on graphene, we measured the PL response as a function of temperature and excitation power, as shown in Figure 4a–h. In this study, we compared the PL response of two samples with different growth durations. Sample A was grown for 100 min (see Figure 4a inset), and sample B was grown for 250 min (see Figure 4b inset).

Figure 4a demonstrates the room temperature PL response of sample A. At room temperature, we observe a broad PL peak centered at 1.52 eV and a lower energy shoulder at 1.42 eV. The peak positions does not change with the increase in laser power. The relation between the PL intensity and laser power is linear for the two peaks (see Figure S5a), thus indicating a high density of states.⁶⁹ Figure 4b shows the room temperature PL response for sample B, and we observe a broad PL peak at 1.45 eV, which undergoes a slight redshift with increasing laser power. The PL emission could be a combination of peaks that behave differently upon increasing

the laser power, which could potentially lead to the observed redshift.

Figure 4c depicts the PL spectra of sample A as a function of temperature. When the temperature is decreased from 300 to 200 K, the peak at 1.52 eV is quenched, whereas the shoulder peak at 1.42 eV becomes prominent. This behavior is attributed to the fact that at room temperature the thermal energy allows high-energy transitions. At lower temperatures, the high-energy transition is quenched, and the low-energy transition is favored.⁷⁰ The PL response is consistent with the study done by Kimball et al., where they observed quenching of the peak at 1.5 eV around 200 K.¹⁰ We additionally measured the power dependence PL of sample A at 200 K (see Figure S5b); the peak position does not change with increasing laser power, and the peak has a tail in the high-energy side. Such power dependence and line shape of PL peak are indicative of band-to-band recombinations.⁷¹ Figure 4d represents the PL spectra of sample B as a function of temperature. When the temperature is decreased from 300 to 260 K, the peak at 1.45 eV is blueshifted to 1.46 eV. However, an additional peak at 1.53 eV is observed when the temperature is decreased to 200 K, and the main peak is red-shifted to 1.42 eV. This behavior is strikingly different from PL emission observed by Kimball et al., where they observed two distinct peaks only at temperatures above 250 K, and the peak at 1.5 eV was more prominent at higher temperatures.¹⁰

Figure 4e–f shows the PL response as a function of temperature (below 200 K) for samples A and B, respectively. We observe a clear redshift when the temperature is decreased from 150 to 12.1 K for sample A, as shown in Figure 4e. At 150 K, the peak is measured at 1.40 eV, which redshifts to 1.35 eV at 12.1 K. The redshift of the peak at lower temperatures has been previously reported by different groups.^{10,72,73} The positive temperature coefficient of this peak has been

previously speculated to be associated with an indirect transition to higher-lying energy states.⁷³ For sample B, we observed a similar redshift of the peak when the temperature is decreased from 200 to 50 K, as shown in Figure 4f. The peak at 1.42 eV at 200 K redshifts to 1.38 eV at 50 K, whereas the peak at 1.52 eV undergoes a rapid quenching at low temperatures. Additionally, a second smaller peak at 1.26 eV becomes prominent at below 150 K (see Figure 4f). On further decreasing the temperature from 50 to 6.3 K, there is an observable blueshift of the main peak at 1.38–1.40 eV, which is similar to the work done by Briones et al., where below 40 K, major emission bands with negative temperature coefficients emerge and are responsible for the intense PL signal.⁷² The sample grown for shorter growth duration (sample A) lacks the low-temperature blue shift behavior reported by Briones et al.,⁷² but rather has a similar low-temperature response reported by Kimball et al.¹⁰

Figure 4g–h shows the cryogenic PL response as a function of laser power for the samples A and B, respectively. For both the samples at cryogenic temperatures, the PL signal exhibited a significant blueshift as the laser excitation intensity was increased, and this behavior has been previously reported by Briones et al.⁷² The peak at 1.26 eV present in sample B remains constant, and the intensity of the peaks saturates at a higher laser power (see Figure S5c); the nonshifting behavior of the peak at 1.26 eV and its eventual saturation indicate it is a defect related transition.⁶⁹

Given the similarity between the PL study reported in the literature and sample A, we assign the room temperature PL peaks at 1.52 and 1.42 eV to direct and indirect transitions, respectively. Even though the low-temperature behavior of sample B is similar to the one reported by Briones et al.,⁷² the room temperature PL response is significantly different. The dissimilarity between the room temperature PL response of sample A and B is attributed to the presence of defects in sample B, which is evident by the presence of the defect peak at lower temperatures in sample B. Indeed, for a higher growth time and surface coverage, the probability of defect formation is higher in sample B.

CONCLUSION

In summary, we demonstrated the growth of high-quality crystalline Zn_3P_2 on graphene via vdWE using MBE. The growth on graphene is highly sensitive to the growth conditions, and the defects on graphene play an integral role in nucleation and growth. The growth mechanism was outlined by studying the temporal evolution of the Zn_3P_2 flakes. In the initial phase of the growth, lateral growth is more pronounced. In the later stages of growth, with the increase in areal coverage, there is a switch to dominant vertical growth. We attribute this change to the difference in adsorption and diffusion characteristics of the adatoms on graphene and on well-formed Zn_3P_2 layer (at higher areal coverage). XRD and EBSD revealed a preferential growth direction of Zn_3P_2 on graphene. The {101} family of planes were oriented parallel to the surface of graphene, and the preferential orientation was maintained irrespective of growth duration. The PL response of Zn_3P_2 on graphene as a function of temperature and power is consistent with the optical behavior reported in the literature for Zn_3P_2 grown using different techniques. We compared the PL response of two samples grown for different durations. The difference in the PL behavior between the two samples is attributed to the presence of defects in the sample grown for

longer duration. This work demonstrates an efficient integration of an Earth-abundant material on graphene, which could be used to fabricate Earth-abundant semiconductors and graphene-based solar cells. Future work will be in the direction to improve the growth on van der Waals substrate by reducing the dependence of the growth behavior on the presence of defects on the substrate and to materialize Earth-abundant semiconductor-based devices.

EXPERIMENTAL SECTION

Growth of Zn_3P_2 . The Zn_3P_2 thin films were grown using Veeco GENxplor MBE on the commercially purchased graphene substrate. The graphene substrates were purchased from Graphenea, and each substrate consists of a monolayer of graphene transferred onto a 4-in. SiO_2 (300 nm)/Si (100) wafer. The MBE system utilizes separate sources of zinc and phosphorus (MBE Komponenten GaP-based P_2 source). Before each growth, the graphene substrates were degassed at 500 °C for 1 h in the prep-module. The Zn_3P_2 thin films were grown in the growth-module of the MBE system, at a 150 °C manipulator temperature for 300 min using a Zn BEP of 5.20×10^{-7} Torr and a P_2 BEP of 7.50×10^{-7} Torr.

Photoluminescence Spectroscopy. The spectrometer used for PL is a LabRam HR Evolution HORIBA Raman spectrometer. A source of monochromatic light (laser) of a specific wavelength (532 or 633 nm) is used to investigate the sample. The beam is directed onto the sample using a set of mirrors allowing a controllable alignment. The use of a bandpass filter on the laser's path prevents undesirable laser lines. Neutral density (ND) filters are arranged to tune the laser intensity. After passing through a beam splitter and a dichroic mirror, the laser is focused on the sample. PL spectroscopy is implemented in back reflection geometry, consisting of a collecting signal from the same spot on which the exciting radiation is focused by the lens. The focusing lens has a large numerical aperture in order to collect as much luminescent or scattered light as possible from a large solid angle. The light is then collimated and passes through a notch filter to subtract the overwhelming laser light. It is then focused onto the entrance slit of a spectral device. Light is dispersed into a spectrum by mean of a monochromator. For PL, the diffraction grating holds 300 grooves per millimeter (gr/mm). A charge-coupled device (CDD) detector finally collects the signal.

Raman Spectroscopy. The Raman spectroscopy measurements were done in a commercial Renishaw inVia system at room temperature. A 532 nm laser was used at 1 mW incident power. The backscattered spectrum was collected after an exposure time of 25 s, averaged over 10 accumulations. A diffraction grating of 1800 lines per millimeter (1/mm) was used. The laser spot size used in the measurement was $\sim 1 \mu\text{m}$. the spectral resolution of the setup is 1.5 cm^{-1} .

XRD. The XRD measurement was done using a Panalytical Empyrean XRD setup, which uses a Cu ($\text{K}\alpha$) X-ray source of 1.54 Å.

EBSD. The EBSD maps were acquired with a Nordlys 2 EBSD camera coupled to the Aztec (Oxford Instruments) acquisition software on an XLF30 (FEI) scanning electron microscope working at 25 kV, with a step size of 40 nm, in "refined accuracy" mode to avoid pseudosymmetry miss-indexation issues.

AFM. The AFM measurements were done using a commercial Bruker Dimension FastScan system. A silicon tip mounted on a silicon nitride cantilever was used for the measurements. The scan of each sample was carried out for an area ranging from 1×1 to $5 \times 5 \mu\text{m}^2$ with a frequency range of 1–1.5 Hz. The images were analyzed using Nanoscope software (version 1.7).

Electron Microscopy. The material was characterized using Zeiss Merlin FE-SEM and FEI Talos for conventional TEM operating at 200 kV. The TEM diffraction pattern was indexed using JEMS software, and Gatan software was used to calculate the distance between planes.

■ ASSOCIATED CONTENT

Supporting Information

The Supporting Information is available free of charge at <https://pubs.acs.org/doi/10.1021/acs.cgd.0c00125>.

Additional characterization of the Zn₃P₂ grown on graphene. Raman spectra, XRD measurements, EBSD measurements, and photoluminescence. Effect of total flux is also reported (PDF)

■ AUTHOR INFORMATION

Corresponding Author

Anna Fontcuberta i Morral – Laboratory of Semiconductor Materials, Institute of Materials, School of Engineering and Institute of Physics, School of Basic Sciences, Ecole Polytechnique Fédérale de Lausanne, 1015 Lausanne, Switzerland; orcid.org/0000-0002-5070-2196; Email: anna.fontcuberta-morral@epfl.ch

Authors

Rajrupa Paul – Laboratory of Semiconductor Materials, Institute of Materials, School of Engineering, Ecole Polytechnique Fédérale de Lausanne, 1015 Lausanne, Switzerland; orcid.org/0000-0002-7532-5593

Nicolas Humblot – Laboratory of Semiconductor Materials, Institute of Materials, School of Engineering, Ecole Polytechnique Fédérale de Lausanne, 1015 Lausanne, Switzerland; Division of Physics and Applied Physics, School of Physical and Mathematical Sciences, Nanyang Technological University, 637371, Singapore

Simon Escobar Steinvall – Laboratory of Semiconductor Materials, Institute of Materials, School of Engineering, Ecole Polytechnique Fédérale de Lausanne, 1015 Lausanne, Switzerland

Elias Zsolt Stutz – Laboratory of Semiconductor Materials, Institute of Materials, School of Engineering, Ecole Polytechnique Fédérale de Lausanne, 1015 Lausanne, Switzerland

Shreyas Sanjay Joglekar – Laboratory of Semiconductor Materials, Institute of Materials, School of Engineering, Ecole Polytechnique Fédérale de Lausanne, 1015 Lausanne, Switzerland

Jean-Baptiste Leran – Laboratory of Semiconductor Materials, Institute of Materials, School of Engineering, Ecole Polytechnique Fédérale de Lausanne, 1015 Lausanne, Switzerland

Mahdi Zamani – Laboratory of Semiconductor Materials, Institute of Materials, School of Engineering, Ecole Polytechnique Fédérale de Lausanne, 1015 Lausanne, Switzerland

Cyril Cayron – Laboratory of Thermomechanical Metallurgy, School of Engineering, Ecole Polytechnique Fédérale de Lausanne, 2002 Neuchâtel, Switzerland

Roland Logé – Laboratory of Thermomechanical Metallurgy, School of Engineering, Ecole Polytechnique Fédérale de Lausanne, 2002 Neuchâtel, Switzerland

Andres Granados del Aguila – Division of Physics and Applied Physics, School of Physical and Mathematical Sciences, Nanyang Technological University, 637371, Singapore; orcid.org/0000-0002-8162-7192

Qihua Xiong – Division of Physics and Applied Physics, School of Physical and Mathematical Sciences, Nanyang Technological University, 637371, Singapore; orcid.org/0000-0002-2555-4363

Complete contact information is available at: <https://pubs.acs.org/doi/10.1021/acs.cgd.0c00125>

Notes

The authors declare no competing financial interest.

■ ACKNOWLEDGMENTS

Authors acknowledge funding from the SNF Consolidator Grant (BSCGI0-157705). Q.X. gratefully acknowledges the support from Ministry of Education by AcRF Tier1 grants (RG194/117). A.G.d.A. gratefully acknowledges the financial support of the Presidential Postdoctoral Fellowship program of the Nanyang Technological University.

■ REFERENCES

- (1) Wadia, C.; Alivisatos, A. P.; Kammen, D. M. Materials Availability Expands the Opportunity for Large-Scale Photovoltaics Deployment. *Environ. Sci. Technol.* **2009**, *43*, 2072–2077.
- (2) Stutz, E. Z.; Friedl, M.; Burgess, T.; Tan, H. H.; Caroff, P.; Jagadish, C.; Fontcuberta i Morral, A. Nanosails Showcasing Zn₃As₂ as an Optoelectronic-Grade Earth Abundant Semiconductor. *Phys. Status Solidi RRL* **2019**, *13*, 1900084.
- (3) Misiewicz, J.; Bryja, L.; Jezierski, K.; Szatkowski, J.; Mirowska, N.; Gumienny, Z.; Placzek-Popko, E. Zn₃P₂—a New Material for Optoelectronic Devices. *Microelectron. J.* **1994**, *25*, xxiii–xxviii.
- (4) Bhushan, M. Schottky Solar Cells on Thin Polycrystalline Zn₃P₂ Films. *Appl. Phys. Lett.* **1982**, *40*, 51–53.
- (5) Escobar Steinvall, S.; Tappy, N.; Ghasemi, M.; Zamani, R. R.; LaGrange, T.; Stutz, E. Z.; Leran, J.-B.; Zamani, M.; Paul, R.; Fontcuberta i Morral, A. Multiple Morphologies and Functionality of Nanowires Made from Earth-Abundant Zinc Phosphide. *Nanoscale Horiz.* **2020**, *5*, 274.
- (6) Fagen, E. A. Optical Properties of Zn₃P₂. *J. Appl. Phys.* **1979**, *50*, 6505–6515.
- (7) Wyeth, N. C.; Catalano, A. Spectral Response Measurements of Minority-carrier Diffusion Length in Zn₃P₂. *J. Appl. Phys.* **1979**, *50*, 1403–1407.
- (8) Shockley, W.; Queisser, H. J. Detailed Balance Limit of Efficiency of P-n Junction Solar Cells. *J. Appl. Phys.* **1961**, *32*, 510–519.
- (9) Pawlikowski, J. M. Absorption Edge of Zn₃P₂. *Phys. Rev. B: Condens. Matter Mater. Phys.* **1982**, *26*, 4711–4713.
- (10) Kimball, G. M.; Müller, A. M.; Lewis, N. S.; Atwater, H. A. Photoluminescence-Based Measurements of the Energy Gap and Diffusion Length of Zn₃P₂. *Appl. Phys. Lett.* **2009**, *95*, 112103.
- (11) Bhushan, M.; Catalano, A. Polycrystalline Zn₃P₂ Schottky Barrier Solar Cells. *Appl. Phys. Lett.* **1981**, *38*, 39–41.
- (12) Pistorius, C. W. F. T.; Clark, J. B.; Coetzer, J.; Kruger, G. J.; Kunze, O. A. High-Pressure Phase Relations And Crystal Structure Determination For Zinc Phosphide, Zn₃P₂, And Cadmium Phosphide, Cd₃P₂. *High Temp. - High Press.* **1977**, *9*, 471–482.
- (13) Bosco, J. P.; Kimball, G. M.; Lewis, N. S.; Atwater, H. A. Pseudomorphic Growth and Strain Relaxation of α -Zn₃P₂ on GaAs(001) by Molecular Beam Epitaxy. *J. Cryst. Growth* **2013**, *363*, 205–210.
- (14) Long, J. The Growth of Zn₃P₂ by Metalorganic Chemical Vapor Deposition. *J. Electrochem. Soc.* **1983**, *130*, 725–728.
- (15) Chu, T. L.; Chu, S. S.; Murthy, K.; Stokes, E. D.; Russell, P. E. Deposition and Properties of Zinc Phosphide Films. *J. Appl. Phys.* **1983**, *54*, 2063–2068.
- (16) Yin, W.-J.; Yan, Y. The Electronic Properties of Point Defects in Earth-Abundant Photovoltaic Material Zn₃P₂: A Hybrid Functional Method Study. *J. Appl. Phys.* **2013**, *113*, No. 013708.
- (17) Demers, S.; van de Walle, A. Intrinsic Defects and Dopability of Zinc Phosphide. *Phys. Rev. B: Condens. Matter Mater. Phys.* **2012**, *85*, 195208.
- (18) Kimball, G. M.; Lewis, N. S.; Atwater, H. A. Direct Evidence of Mg-Zn-P Alloy Formation in Mg/Zn₃P₂ Solar Cells. In *37th IEEE Photovoltaic Specialists Conference*; IEEE: Piscataway, NJ, 2011; pp 3381–3384.

- (19) Koma, A.; Sunouchi, K.; Miyajima, T. Fabrication and Characterization of Heterostructures with Subnanometer Thickness. *Microelectron. Eng.* **1984**, *2*, 129–136.
- (20) Xia, W.; Dai, L.; Yu, P.; Tong, X.; Song, W.; Zhang, G.; Wang, Z. Recent Progress in van Der Waals Heterojunctions. *Nanoscale* **2017**, *9*, 4324–4365.
- (21) Walsh, L. A.; Van Der Hinkle, C. L. Waals Epitaxy: 2D Materials and Topological Insulators. *Appl. Mater. Today* **2017**, *9*, 504–515.
- (22) Orlita, M.; Faugeras, C.; Plochocka, P.; Neugebauer, P.; Martinez, G.; Maude, D. K.; Barra, A.-L.; Sprinkle, M.; Berger, C.; de Heer, W. A.; Potemski, M. Approaching the Dirac Point in High-Mobility Multilayer Epitaxial Graphene. *Phys. Rev. Lett.* **2008**, *101*, 267601.
- (23) Balandin, A. A.; Ghosh, S.; Bao, W.; Calizo, I.; Teweldebrhan, D.; Miao, F.; Lau, C. N. Superior Thermal Conductivity of Single-Layer Graphene. *Nano Lett.* **2008**, *8*, 902–907.
- (24) Nair, R. R.; Blake, P.; Grigorenko, A. N.; Novoselov, K. S.; Booth, T. J.; Stauber, T.; Peres, N. M. R.; Geim, A. K. Fine Structure Constant Defines Visual Transparency of Graphene. *Science* **2008**, *320*, 1308–1308.
- (25) Lee, C.; Wei, X.; Kysar, J. W.; Hone, J. Measurement of the Elastic Properties and Intrinsic Strength of Monolayer Graphene. *Science* **2008**, *321*, 385–388.
- (26) Mohseni, P. K.; Behnam, A.; Wood, J. D.; Zhao, X.; Yu, K. J.; Wang, N. C.; Rockett, A.; Rogers, J. A.; Lyding, J. W.; Pop, E.; Li, X. Monolithic III-V Nanowire Solar Cells on Graphene via Direct van Der Waals Epitaxy. *Adv. Mater.* **2014**, *26*, 3755–3760.
- (27) Chung, K.; Yoo, H.; Hyun, J. K.; Oh, H.; Tchoe, Y.; Lee, K.; Baek, H.; Kim, M.; Yi, G.-C. Flexible GaN Light-Emitting Diodes Using GaN Microdisks Epitaxially Laterally Overgrown on Graphene Dots. *Adv. Mater.* **2016**, *28*, 7688–7694.
- (28) Bae, S.; Kim, H.; Lee, Y.; Xu, X.; Park, J.-S.; Zheng, Y.; Balakrishnan, J.; Lei, T.; Kim, H. R.; Song, Y. I.; Kim, Y.-J.; Kim, K. S.; Özyilmaz, B.; Ahn, J.-H.; Hong, B. H.; Iijima, S. Roll-to-Roll Production of 30-Inch Graphene Films for Transparent Electrodes. *Nat. Nanotechnol.* **2010**, *5*, 574–578.
- (29) Juang, Z.-Y.; Wu, C.-Y.; Lu, A.-Y.; Su, C.-Y.; Leou, K.-C.; Chen, F.-R.; Tsai, C.-H. Graphene Synthesis by Chemical Vapor Deposition and Transfer by a Roll-to-Roll Process. *Carbon* **2010**, *48*, 3169–3174.
- (30) Vazquez-Mena, O.; Bosco, J. P.; Ergen, O.; Rasool, H. I.; Fathalizadeh, A.; Tosun, M.; Crommie, M.; Javey, A.; Atwater, H. A.; Zettl, A. Performance Enhancement of a Graphene-Zinc Phosphide Solar Cell Using the Electric Field-Effect. *Nano Lett.* **2014**, *14*, 4280–4285.
- (31) Suda, T.; Kakishita, K.; Sato, H.; Sasaki, K. N-type Zinc Phosphide Grown by Molecular Beam Epitaxy. *Appl. Phys. Lett.* **1996**, *69*, 2426–2428.
- (32) Foxon, C. T. Three Decades of Molecular Beam Epitaxy. *J. Cryst. Growth* **2003**, *251*, 1–8.
- (33) Joyce, B. A.; Joyce, T. B. Basic Studies of Molecular Beam Epitaxy—Past, Present and Some Future Directions. *J. Cryst. Growth* **2004**, *264*, 605–619.
- (34) Ghasemi, M.; Stutz, E.; Escobar Steinvall, S.; Zamani, M.; Fontcuberta i Morral, A. Thermodynamic Re-Assessment of the Zn–P Binary System. *Materialia* **2019**, *6*, 100301.
- (35) Pangilinan, G.; Sooryakumar, R.; Misiewicz, J. Raman Activity of Zn₃P₂. *Phys. Rev. B: Condens. Matter Mater. Phys.* **1991**, *44*, 2582–2588.
- (36) Misiewicz, J. Inter-Band Transitions in Zn₃P₂. *J. Phys.: Condens. Matter* **1990**, *2*, 2053–2072.
- (37) Niraula, D.; McCulloch, J.; Warrell, G. R.; Irving, R.; Karpov, V. G.; Shvydka, D. Electric Field Stimulated Growth of Zn Whiskers. *AIP Adv.* **2016**, *6*, No. 075201.
- (38) Nakada, K.; Ishii, A. Migration of Adatom Adsorption on Graphene Using DFT Calculation. *Solid State Commun.* **2011**, *151*, 13–16.
- (39) Ishii, A.; Yamamoto, M.; Asano, H.; Fujiwara, K. DFT Calculation for Adatom Adsorption on Graphene Sheet as a Prototype of Carbon Nanotube Functionalization. *J. Phys. Conf. Ser.* **2008**, *100*, No. 052087.
- (40) Alaskar, Y.; Arafin, S.; Wickramaratne, D.; Zurbuchen, M. A.; He, L.; McKay, J.; Lin, Q.; Goorsky, M. S.; Lake, R. K.; Wang, K. L. Towards van Der Waals Epitaxial Growth of GaAs on Si Using a Graphene Buffer Layer. *Adv. Funct. Mater.* **2014**, *24*, 6629–6638.
- (41) Mukherjee, S.; Nateghi, N.; Jacobberger, R. M.; Bouthillier, E.; de la Mata, M.; Arbiol, J.; Coenen, T.; Cardinal, D.; Levesque, P.; Desjardins, P.; Martel, R.; Arnold, M. S.; Moutanabbir, O. Growth and Luminescence of Polytropic InP on Epitaxial Graphene. *Adv. Funct. Mater.* **2018**, *28*, 1705592.
- (42) Wofford, J. M.; Nie, S.; McCarty, K. F.; Bartelt, N. C.; Dubon, O. D. Graphene Islands on Cu Foils: The Interplay between Shape, Orientation, and Defects. *Nano Lett.* **2010**, *10*, 4890–4896.
- (43) Banhart, F.; Kotakoski, J.; Krashenninnikov, A. V. Structural Defects in Graphene. *ACS Nano* **2011**, *5*, 26–41.
- (44) Lee, S.-M.; Kim, J.-H.; Ahn, J.-H. Graphene as a Flexible Electronic Material: Mechanical Limitations by Defect Formation and Efforts to Overcome. *Mater. Today* **2015**, *18*, 336–344.
- (45) Yu, S. U.; Park, B.; Cho, Y.; Hyun, S.; Kim, J. K.; Kim, K. S. Simultaneous Visualization of Graphene Grain Boundaries and Wrinkles with Structural Information by Gold Deposition. *ACS Nano* **2014**, *8*, 8662–8668.
- (46) Meyer, J. C.; Kisielowski, C.; Erni, R.; Rossell, M. D.; Crommie, M. F.; Zettl, A. Direct Imaging of Lattice Atoms and Topological Defects in Graphene Membranes. *Nano Lett.* **2008**, *8*, 3582–3586.
- (47) Heilmann, M.; Munshi, A. M.; Sarau, G.; Göbel, M.; Tessarek, C.; Fauske, V. T.; van Helvoort, A. T. J.; Yang, J.; Latzel, M.; Hoffmann, B.; Conibeer, G.; Weman, H.; Christiansen, S. Vertically Oriented Growth of GaN Nanorods on Si Using Graphene as an Atomically Thin Buffer Layer. *Nano Lett.* **2016**, *16*, 3524–3532.
- (48) Zeng, Q.; Chen, Z.; Zhao, Y.; Wei, T.; Chen, X.; Zhang, Y.; Yuan, G.; Li, J. Graphene-Assisted Growth of High-Quality AlN by Metalorganic Chemical Vapor Deposition. *Jpn. J. Appl. Phys.* **2016**, *55*, No. 085501.
- (49) Zhou, H.; Qiu, C.; Liu, Z.; Yang, H.; Hu, L.; Liu, J.; Yang, H.; Gu, C.; Sun, L. Thickness-Dependent Morphologies of Gold on N-Layer Graphenes. *J. Am. Chem. Soc.* **2010**, *132*, 944–946.
- (50) Kim, Y.; Moyon, E.; Yi, H.; Avila, J.; Chen, C.; Asensio, M. C.; Lee, Y. H.; Pribat, D. Synthesis of High Quality Graphene on Capped (111) Cu Thin Films Obtained by High Temperature Secondary Grain Growth on c-Plane Sapphire Substrates. *2D Mater.* **2018**, *5*, No. 035008.
- (51) Chen, C.; Avila, J.; Asensio, M. C. Chemical and Electronic Structure Imaging of Graphene on Cu: A NanoARPES Study. *J. Phys.: Condens. Matter* **2017**, *29*, 183001.
- (52) Wang, X.; Tabakman, S. M.; Dai, H. Atomic Layer Deposition of Metal Oxides on Pristine and Functionalized Graphene. *J. Am. Chem. Soc.* **2008**, *130*, 8152–8153.
- (53) Liu, Y.; Weinert, M.; Li, L. Spiral Growth without Dislocations: Molecular Beam Epitaxy of the Topological Insulator Bi₂Se₃ on Epitaxial Graphene/SiC(0001). *Phys. Rev. Lett.* **2012**, *108*, 115501.
- (54) Harrison, S. E.; Li, S.; Huo, Y.; Zhou, B.; Chen, Y. L.; Harris, J. S. Two-Step Growth of High Quality Bi₂Te₃ Thin Films on Al₂O₃ (0001) by Molecular Beam Epitaxy. *Appl. Phys. Lett.* **2013**, *102*, 171906.
- (55) Ferhat, M.; Tedenac, J. C.; Nagao, J. Mechanisms of Spiral Growth in Bi₂Te₃ Thin Films Grown by the Hot-Wall-Epitaxy Technique. *J. Cryst. Growth* **2000**, *218*, 250–258.
- (56) Karma, A.; Plapp, M. Spiral Surface Growth without Desorption. *Phys. Rev. Lett.* **1998**, *81*, 4444–4447.
- (57) Nie, Y.; Liang, C.; Cha, P.-R.; Colombo, L.; Wallace, R. M.; Cho, K. A Kinetic Monte Carlo Simulation Method of van Der Waals Epitaxy for Atomistic Nucleation-Growth Processes of Transition Metal Dichalcogenides. *Sci. Rep.* **2017**, *7*, 1–13.
- (58) Politi, P.; Villain, J. Ehrlich-Schwoebel Instability in Molecular-Beam Epitaxy: A Minimal Model. *Phys. Rev. B: Condens. Matter Mater. Phys.* **1996**, *54*, 5114–5129.

(59) Shi, L.; Zhuo, S.; Abulikemu, M.; Mettela, G.; Palaniselvam, T.; Rasul, S.; Tang, B.; Yan, B.; Saleh, N. B.; Wang, P. Annealing Temperature Effects on Photoelectrochemical Performance of Bismuth Vanadate Thin Film Photoelectrodes. *RSC Adv.* **2018**, *8*, 29179–29188.

(60) Sathyamoorthy, R.; Sharmila, C.; Natarajan, K.; Velumani, S. Influence of Annealing on Structural and Optical Properties of Zn₃P₂ Thin Films. *Mater. Charact.* **2007**, *58*, 745–749.

(61) Zanin, I. E.; Aleinikova, K. B.; Antipin, M. Yu.; Afanas'ev, M. M. Analysis of Chemical Bonding in Zn₃P₂ Crystals from X-Ray Diffraction Data. *Crystallogr. Rep.* **2004**, *49*, 579–584.

(62) Zanin, I. E.; Aleinikova, K. B.; Afanasiev, M. M.; Antipin, M. Yu. Structure of Zn₃P₂. *J. Struct. Chem.* **2004**, *45*, 844–848.

(63) Munshi, A. M.; Dheeraj, D. L.; Fauske, V. T.; Kim, D.-C.; van Helvoort, A. T. J.; Fimland, B.-O.; Weman, H. Vertically Aligned GaAs Nanowires on Graphite and Few-Layer Graphene: Generic Model and Epitaxial Growth. *Nano Lett.* **2012**, *12*, 4570–4576.

(64) Johansson, J.; Karlsson, L. S.; Svensson, C. P. T.; Mårtensson, T.; Wacaser, B. A.; Deppert, K.; Samuelson, L.; Seifert, W. Structural Properties of <111> B-Oriented III–V Nanowires. *Nat. Mater.* **2006**, *5*, 574–580.

(65) Schmidt, V.; Wittemann, J. V.; Senz, S.; Gösele, U. Silicon Nanowires: A Review on Aspects of Their Growth and Their Electrical Properties. *Adv. Mater.* **2009**, *21*, 2681–2702.

(66) Katsube, R.; Nose, Y. Orientation of Zn₃P₂ Films via Phosphidation of Zn Precursors. *J. Cryst. Growth* **2017**, *459*, 95–99.

(67) Pawlikowski, J. M.; Misiewicz, J.; Mirowska, N. Direct and Indirect Optical Transitions in Zn₃P₂. *J. Phys. Chem. Solids* **1979**, *40*, 1027–1033.

(68) Munoz, V.; Decroix, D.; Chevy, A.; Besson, J. M. Optical Properties of Zinc Phosphide. *J. Appl. Phys.* **1986**, *60*, 3282–3288.

(69) Schmidt, T.; Lischka, K.; Zulehner, W. Excitation-Power Dependence of the near-Band-Edge Photoluminescence of Semiconductors. *Phys. Rev. B: Condens. Matter Mater. Phys.* **1992**, *45*, 8989–8994.

(70) Sun, X.; Liu, J.; Kimerling, L. C.; Michel, J. Direct Gap Photoluminescence of N-Type Tensile-Strained Ge-on-Si. *Appl. Phys. Lett.* **2009**, *95*, No. 011911.

(71) Fu, Y.; Willander, M.; Chen, G. B.; Ji, Y. L.; Lu, W. Photoluminescence Spectra of Doped GaAs Films. *Appl. Phys. A: Mater. Sci. Process.* **2004**, *79*, 619–623.

(72) Briones, F.; Wang, F.; Bube, R. H. Pair Transitions in Zn₃P₂. *Appl. Phys. Lett.* **1981**, *39*, 805–807.

(73) Kurbatov, L. N.; Dirochka, A. I.; Sinitsyn, E. V.; Lazarev, V. B.; Shevchenko, V. Y.; Kozlov, S. E. Luminescence of Cadmium and Zinc Phosphides. *Sov. J. Quantum Electron.* **1976**, *6*, 166.